Journal of Thermal Analysis and Calorimetry (2020) 139:755–764
https://doi.org/10.1007/s10973-019-08402-6

A numerical investigation on the heat transfer characteristics of nanofluid flow in a three-dimensional microchannel with harmonic rotating vortex generators

Y. Amini[1] · S. Akhavan[1] · E. Izadpanah[1]

Received: 4 March 2019 / Accepted: 20 May 2019 / Published online: 28 May 2019

Abstract
Three-dimensional numerical simulation of conjugate heat transfer in a microchannel involving harmonic rotating longitudinal vortex generators is performed. The Al_2O_3–water nanofluid with concentration of 0.5% of volume fraction is used. The mean diameter of particles is 29 nm. The Nusselt number and Fanning friction factor of the microchannel changes are investigated for different Reynolds numbers, rotation frequency, and rotation's direction. Results show that time variations of Nusselt number and friction factor are periodic and their frequencies are the same as vortex generator's rotation frequencies. It was observed that the amplitude of Nusselt number increases with increasing Reynolds number. Furthermore, when all the vortex generators are rotating in the same direction, the amplitudes of Nusselt number and friction factor are higher than when they are rotating in opposite directions.

Keywords Microchannel · Rotational vortex generators · Nanofluids · Fluid flow · Heat transfer

Introduction

By further developing in the technology, the size minimization of thermodynamic systems is attracted more attentions. Recently microchannels have studied by many researchers because of extensively use in electronic cooling industries, medical devices, chemical heat exchanger apparatus, laser equipment, and aerospace industries. Both gas and liquid coolants have been used as working fluid in this type of heat exchangers. However, the latter usually is used for the sake of providing higher heat transfer rates. Tuckerman and Pease [1] introduced rectangular water-cooled microchannels for cooling very large scale-integrated (VLSI) circuits in 1981. Their experiments showed that by using these heatsinks heat transfer rates were increased because of the low thermal resistance of the microchannel.

For analyzing systems in such small sizes, it is essential to explain the effects of channel size on fluid flow characteristics. The experimental studies presented by Xu et al. [2] show that conventional Navier–Stokes equations are reliable to predict flow characteristics in microchannels with a hydraulic diameter greater than 30 μm. Their results show that the critical Reynolds number (where the transition from laminar to turbulent flow regime happens) decreases if microchannel hydraulic diameter decreases. Many numerical studies have been done by solving the Navier–Stokes equations in microchannels with hydraulic diameter greater than 30 μm. Toh et al. [3] performed a numerical simulation of fluid flow and heat transfer in a rectangular microchannel heatsink and their results show a good agreement with the experimental results of Tuckerman and Pease [1].

The heat transfer rate and pressure drop in microchannels are highly dependent on microchannel geometry [4] and an effective method to increase the heat transfer rate is changing the cross-sectional shape of the microchannel. Moradikazerouni et al. [5] numerically investigated the effects of different microchannel cross sections on the heat extraction from a supercomputer circuit board. Their results show that regardless of manufacturing costs, the

✉ Y. Amini
Aminiyasser@pgu.ac.ir

[1] Department of Mechanical Engineering, Persian Gulf University, Bushehr, Iran

microchannel with triangular cross section provides the highest heat transfer rate for cooling the circuit. Zho et al. [6] numerically studied convective heat transfer in microchannels with different cross sections (e.g., trapezoidal and triangular). They reported that a trapezoidal microchannel has higher heat transfer rates compared to a triangular microchannel. Dehghan et al. [7] numerically investigated the effects of tapered flow passage on the heat transfer and fluid flow in a microchannel. Their results show that the flow passage tapering can increase the Poiseuille number and decrease the pressure drop. The most efficient tapering ratio was found to be 0.5. Using obstructions that can generate vortexes and secondary flows in the microchannel is another conventional method to increase heat transfer rates and microchannel efficiency. These obstructions can be in any shape (ribs [8, 9], wings, winglets [10] and vortex generators [11]), and the basis of their work is fluid mixing. Ghani et al. [12] investigated heat transfer and fluid flow in a microchannel with sinusoidal cavities and rectangular ribs. They reported that using these configuration leads to much higher heat transfer rates compared to using only sinusoidal cavities or rectangular ribs. Datta et al. [13] numerically investigated convective heat transfer in a rectangular microchannel with longitudinal vortex generators (LVGs) in Reynolds number range of 200–1100. They showed that for Reynolds numbers greater than 600, the optimum angle of LVGs is 30°. For lower Reynolds number, they suggested higher inclination angles. Ebrahimi et al. [14] studied the heat transfer in a microchannel with two LVGs. They considered different LVGs angle of attacks and showed that using VGs can enhance the heat transfer by 2–30%.

To further increase the heat transfer rate and overall performance of microchannels, it is needed to use working fluids with superior thermophysical properties. Recently nanofluids are widely used in thermodynamic systems like photovoltaic systems [15], solar collectors [16], electronic system cooling [17–19], and miniaturized systems [20, 21] because of providing higher heat transfer rates and fluid stability issues. Generally, nanofluids are made of base fluid and nanoparticles. In nanofluids, the thermal properties of the base fluid can be considerably enhanced by nanoparticles [22]. Usually base fluid is water. Common nanoparticles are Al_2O_3, CuO, and TiO_2. Ambreen et al. [23] studied the effects of nanoparticles size on heat transfer and pressure drop in a microchannel. Their results show that by decreasing nanoparticle diameters the heat transfer rate increases in the microchannel because of increasing effective nanoparticle surface area. By decreasing nanoparticle diameters from 200 to 20 nm, a 11% increase in heat transfer rate was observed. Ebrahimi et al. [24, 25] numerically investigated single-phase and two-phase nanofluid flow and heat transfer in a rectangular microchannel with VGs. Their results show a maximum 53.06% increase in heat transfer for the ranges of the parameters in the study. Nitiapiruk et al. [26] experimentally investigated heat transfer and pressure drop in microchannels. They used TiO_2–water nanofluid as working fluid. Three different models were used to calculate the effective viscosity and conductivity of the nanofluid. Their results show that the implemented model has insignificant effects on the calculated Nusselt number, but it can considerably affect the calculated friction factor. Hence, they propose that the friction factor must be evaluated by the viscosity obtained from experimental results. Taffarroj et al. [27] used neural network to predict the heat transfer rate and Nusselt number of TiO_2–water nanofluid flow in microchannels. Based on the results, the average deviation between predicted and experimented Nusselt number was 0.3% which is negligible. Therefore, in the design point of view, a well-trained neural network is very efficient to precisely predict the heat transfer rate in a microchannel.

Most of the researches mentioned above use a passive method (using nanofluids or stationary vortex generators) to enhance heat transfer in a microchannel. It is very interesting to investigate the feasibility of enhancing convective heat transfer in a microchannel by using active methods. In the present study, three-dimensional nanofluid flow in a rectangular microchannel containing rotating VGs is simulated by using finite volume method with dynamic mesh motion. Previous studies verify the results. Different Reynolds numbers, frequencies, and rotation modes involving counter clock and clockwise are studied. Moreover, the effects of these parameters on the fluid flow characteristics and performance of heat transfer are investigated.

Problem description

In this study, a microchannel which contained 12 longitudinal vortex generators is considered and shown in Fig. 1. This configuration is studied by many researchers such as [24, 25]. The water-based nanofluid with 0.5% of volume fraction of Al_2O_3 particle is chosen as the working fluid. Since the geometry is symmetric, for reducing the computation time the half of the microchannel is modeled. These LVGs are rotating around the y-axis by a harmonic motion with an amplitude of 10° about their initial angle (30°) with two different rotation frequencies of 5 and 50 Hz. Moreover, the effects of different Reynolds number and rotation modes are examined in this study. In the first rotation mode, all of the VGs rotate in the same direction according to the equation $\theta = A\sin(\omega t)$. Where θ, A, and ω are the angular position of VGs, amplitude of the angular position, and rotation frequency of the VGs,

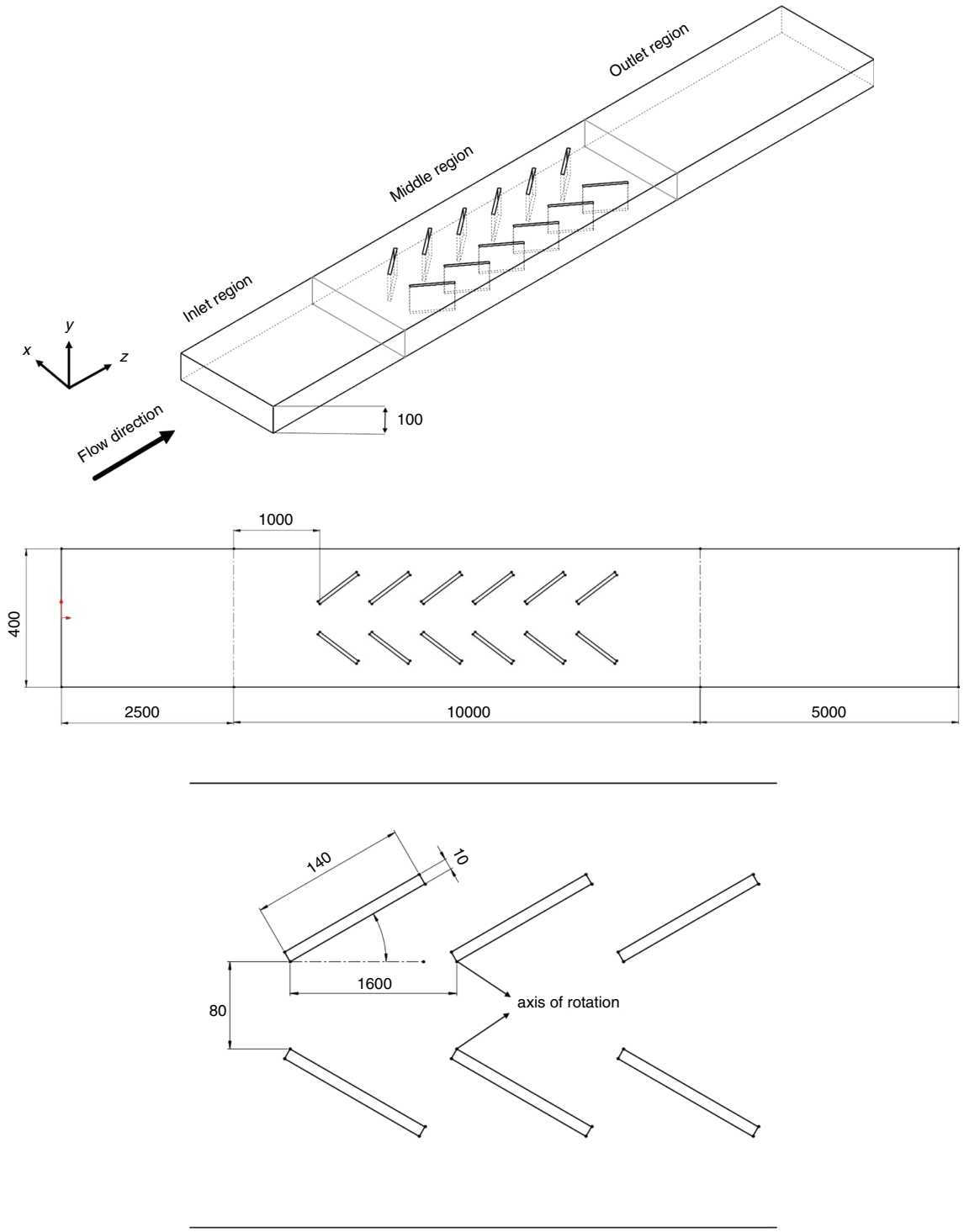

Fig. 1 Schematic of the computational domain (dimensions are in μm)

respectively. In the second mode, every other VGs rotate in the opposite directions with the same value of amplitude and rotation frequency. According to Fig. 1, the domain has three main regions:

- *Inlet region* this region is considered to ensure that flow entering the middle region is fully developed. All of the walls of this region are adiabatic.
- *Middle region* in this region the LVGs are equally spaced as is illustrated in Fig. 1. Constant heat flux

$\left(q'' = 200,000 \frac{\mathrm{w}}{\mathrm{m}^2}\right)$ is implemented on the upper wall of this region. (y-axis is perpendicular to this wall). Other walls of this region are adiabatic.

- *Outlet region* this region is considered to prevent backflow. All of the walls of this region are adiabatic.

Model formulation and numerical analysis: single-phase model

In this study, the microchannel is chosen to be made up of silicon [28, 29]. The working fluid is water-based nanofluid with 0.5% volume fraction of Al_2O_3 nanoparticles. The flow regime is laminar and Reynolds number range is between 50 and 250. The rotation of LVGs makes the problem unsteady and the time step value of 1e−5 s is used. In order to capture the thermal and hydrodynamic gradients near the solid walls, the grid is fined enough near these walls. The PISO algorithm is chosen as pressure–velocity coupling method. For an unsteady flow, the continuity, momentum, and energy equations can be written as below [30]:

$$\frac{\partial}{\partial x_\mathrm{i}}(V_\mathrm{i}) = 0 \tag{1}$$

$$\rho \frac{DV_\mathrm{i}}{Dt} = \frac{\partial \tau_\mathrm{ij}}{\partial x_\mathrm{i}} - \frac{\partial P}{\partial x_\mathrm{i}} \tag{2}$$

$$\rho c_\mathrm{p} \frac{DT_\mathrm{f}}{\mathrm{d}t} = \frac{\partial}{\partial x_\mathrm{i}}\left(k \frac{\partial T_\mathrm{f}}{\partial x_\mathrm{i}}\right) + \varphi \tag{3}$$

where ρ,V, P, and μ are density, velocity, pressure, and fluid viscosity, respectively. Furthermore, T and k are temperature and conductivity of the fluid. φ is viscous dissipation term, and for an incompressible flow it is as following:

$$\varphi = \tau_\mathrm{ij} \frac{\partial V_\mathrm{i}}{\partial x_\mathrm{j}} \tag{4}$$

$$\tau_\mathrm{ij} = \mu\left(\frac{\partial V_\mathrm{i}}{\partial x_\mathrm{j}} + \frac{\partial V_\mathrm{j}}{\partial x_\mathrm{i}}\right) \tag{5}$$

Natural convection, radiation, and viscous dissipation are neglected in this simulation [31]. Since the conjugated heat transfer will be modeled in this study, the energy equation needs to be solved for solid zones. The governing equation for conduction in the solid zones is as follows:

$$\nabla^2 T_\mathrm{s} = 0 \tag{6}$$

In single-phase modeling, the nanoparticles and water are considered to be homogeneous, and the thermophysical properties (viscosity and conductivity of fluid) of water and nanoparticles are assumed to vary with temperature. These variations are presented in Table 1.

Table 1 Thermophysical properties of nanoparticles, pure water, and silicon

	Al_2O_3 [32]	Silicon [33]	Pure water [34]
μ/Pa s			$2.761 \times 10^{-6} \exp\left(\frac{1713}{T}\right)$
K/w m^{-1} k^{-1}	36	$290 - 0.4\ T$	$0.6\left(1 + 4.167 \times 10^{-5} T\right)$
C_p/J kg^{-1} k^{-1}	765	$390 + 0.9\ T$	4180
ρ/kg m^{-3}	3970	2330	1000

Using the mixture model [35], one can calculate the density of nanofluid as following:

$$\rho_\mathrm{nf} = (1 - \alpha)\rho_\mathrm{bf} + \alpha \rho_\mathrm{np} \tag{7}$$

where α is the volume fraction of nanoparticles and subscripts nf, bf , and np stand for nanofluid, base fluid, and nanoparticle, respectively. The thermal conductivity of nanofluids can be assumed as the combination of two parts [36]:

$$k_\mathrm{nf} = k_\mathrm{static} + k_\mathrm{brownian} \tag{8}$$

Hamilton–Crosser model [37] can be used to obtain k_static and k_brownian:

$$k_\mathrm{static} = k_\mathrm{bf}\left[\frac{(k_\mathrm{np,eff} + 2k_\mathrm{bf}) - 2\alpha\left(k_\mathrm{bf} - k_\mathrm{np,eff}\right)}{(k_\mathrm{np,eff} + 2k_\mathrm{bf}) - \alpha\left(k_\mathrm{bf} - k_\mathrm{np,eff}\right)}\right] \tag{9}$$

$$k_\mathrm{brownian} = 5 \times 10^4 \alpha C_\mathrm{p.bf} \rho_\mathrm{bf} \sqrt{\frac{k_\mathrm{b} T}{d_\mathrm{np} \rho_\mathrm{np}}}\, g\left(T, \alpha, d_\mathrm{np}\right) \tag{10}$$

where k_b is Boltzmann constant and equals to $1.3806503 \times 10^{-23}$ J k^{-1}.

The term $k_\mathrm{np.eff}$ accounts for the effects of interfacial thermal resistance and can be calculated by the following equation.

$$k_\mathrm{np,eff} = \frac{d_\mathrm{np}}{R_\mathrm{b} + \left(d_\mathrm{np}/k_\mathrm{np}\right)} \tag{11}$$

where R_b is Kapitza resistance ($4 \times 10^{-8}\ \mathrm{km}^2\ \mathrm{W}^{-1}$). Similar to Eq. (9), the effective viscosity can be obtained by the following equation:

$$\mu_\mathrm{nf} = \mu_\mathrm{static} + \mu_\mathrm{brownian} \tag{12}$$

$$\mu_\mathrm{static} = \frac{\mu_\mathrm{bf}}{(1 - \alpha)^{\frac{5}{2}}} \tag{13}$$

$$\mu_\mathrm{brownian} = 5 \times 10^4 \alpha \rho_\mathrm{bf} \sqrt{\frac{k_\mathrm{b} T}{d_\mathrm{np} \rho_\mathrm{np}}}\, g\left(T, \alpha, d_\mathrm{np}\right) \tag{14}$$

The function g is a semiempirical relation for water–Al_2O_3 nanofluid. This relation can be obtained by fitting experimental data sets as follows [38].

$$g = \left[\left(a + b\ln(d_{np}) + c\ln(\alpha) + d\ln(\alpha)\ln(d_{np}) + e\ln(d_{np})^2\right)\right] \ln(T) + \left[m + h\ln(d_{np}) + i\ln(\alpha) + j\ln(\alpha)\ln(d_{np}) + k\ln(d_{np})^2\right] \quad (15)$$

The coefficients a to k are listed in Table 2.

The Reynolds number (Re) and hydraulic diameter (D_h) of the microchannel are defined as follows:

$$Re = \frac{\rho v D_h}{\mu} \quad (16)$$

$$D_h = \frac{2ab}{a+b} \quad (17)$$

All the properties and velocity used in Eq. 16 are evaluated from the inlet section. In Eq. 18 a and b are the length and width of the cross section of the microchannel, respectively. According to [34, 39], the heat transfer coefficient (h) and Nusselt (Nu) number can be calculated by the below equations:

$$h = \frac{q''}{\bar{T}_{hw} - (T_{inlet} + T_{outlet})/2} \quad (18)$$

$$Nu = \frac{hD_h}{\bar{k}_{bf}} \quad (19)$$

where q'' represents the heat flux, $\bar{T}_{hw}$ is the mean wall temperature, and T_{inlet} and T_{outlet} are inlet and outlet bulk temperature of the heated zone of the geometry. Thermal conductivity k appearing in Eq. 19 is measured at the arithmetic mean temperature of the inlet and outlet.

Using nanofluids can increase heat transfer intensity by enhancing the thermal conductivity of the working fluid. Moreover, nanoparticles can increase the fluid viscosity leading to higher pressure drop in the microchannel. To evaluate the overall performance of nanofluids and rotating VG's (which considers both heat transfer enhancement and pressure drop increase), following equation can be used [14, 24, 32, 40, 41]:

Table 2 Parameters used in Eq. 15

Coefficient values	Water–Al_2O_3
a	52.813
b	6.115
c	0.695
d	0.041
e	0.176
g	− 298.198
h	− 34.532
i	− 3.922
j	− 0.235
k	− 0.999

$$\eta = \left(\frac{Nu}{Nu_{bf}}\right)\left(\frac{f_{bf}}{f}\right)^{\frac{1}{3}} \quad (20)$$

where Nu_{bf} and f_{bf} are the Nusselt number and Fanning friction factor of the microchannel with pure water. The parameter η gives a quantitative feedback that whether using nanofluids is an advantage or disadvantage.

Model validation

In this section, the implemented model is verified. Four grids with different sizes are used to ensure the mesh independence of the results. The test is carried out using stationary VGs and Reynolds number of 100. The working fluid is water–Al_2O_3 nanofluid with nanoparticle concentrations of 0.5%.

Table 3 compares the calculated averaged Nusselt numbers and friction factor for different grid sizes. According to this table, by refining the grid from 700,000 to 1,000,000, the deviation of the results falls behind 0.5%. Hence, the grid with 1,000,000 cells is chosen for modeling the problem.

To validate the employed numerical model with the literature, numerical data from Ref. [24] for pure water and water–Al_2O_3 nanofluid with volume fractions of 0.5%, 1%, and 2% flowing through a rectangular microchannel with 160 nm hydraulic diameter in different Reynolds number (Re) are used. Nanoparticle diameter of 29 nm is chosen. Average Nusselt number (Nu) and Fanning friction factor (f) are compared to the results obtained by Ref. [24]. This comparison is shown in Figs. 2 and 3, and it is observed that the present numerical results are in a good agreement with presented values by Ebrahimi et al. [24].

In order to validate the dynamic mesh motion of LVGs, the lift and the drag coefficients of a pitching airfoil are compared with experimental data of Lee and Gerontakos [42] and numerical results given by Gharali and Johnson [43]. In Fig. 4a, b, the calculated lift and drag coefficients are compared with experimental data of Lee and Gerontakos [42] and numerical data of Gharali and Johnson [43]. At the up-stroke motion of airfoil, both numerical results are in good agreement with experimental results. However, at the down-stroke motion; the current lift and drag are closer to the experimental data than that of Gharali and Johnson [43].

Table 3 Grid independence test results

Grid size	Nu	f
400,000	6.039	0.962
500,000	5.751	0.921
700,000	5.663	0.911
1,000,000	5.634	0.908

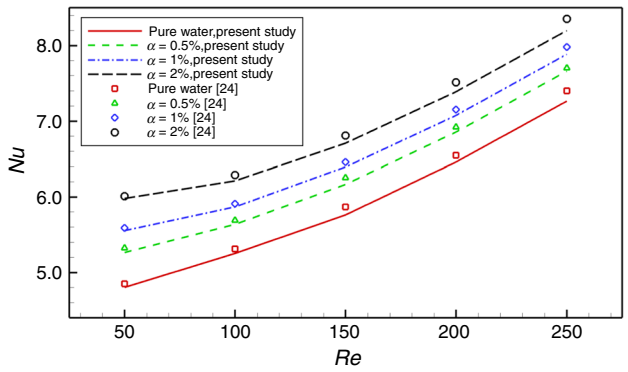

Fig. 2 Comparison of present *Nu* number with results of Ref. [24]

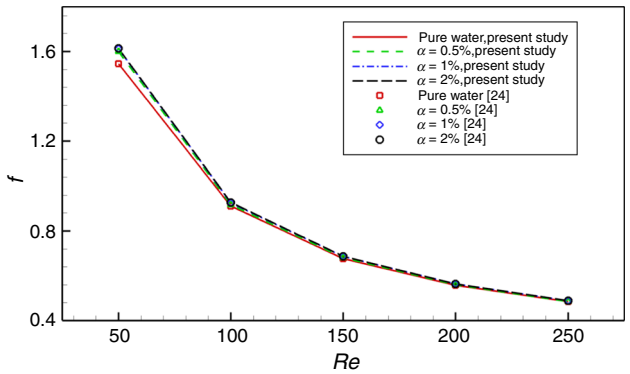

Fig. 3 Comparison of present *f* values with results of Ref. [24]

Results and discussion

In Figs. 5 and 6, the time history of Nusselt number and Fanning friction factor is presented versus dimensionless time (t/τ) where τ is the period of rotation of VGs and it is equal to $\tau = 2\pi/\omega$. In these figures, Reynolds number is 200 and rotation frequencies of LVGs are 5 and 50 Hz. As can be seen, when LVGs are rotating, the variation of Nusselt number and friction factor for both frequencies has harmonic behavior. In the case of the same direction of rotation of the VGs, all of the VGs reach the maximum angular position together and the thermal boundary layer thickness decreases along the constant heat flux wall leading to much higher Nusselt number in this moment. Conversely, in the case of the opposite direction of the VGs, when a VG is located in its maximum angular position, next VG reaches its minimum position. Hence in one portion of the channel, thermal boundary layer thickness decreases and in the next portion increases. As a result, when the VGs are rotating in the opposite direction, maximum Nusselt number is less than the case that the VGs are rotating in the same direction. Table 4 compares the results of Figs. 5 and 6 quantitatively. A notable point in Fig. 6 is that unlike Nusselt number, time history of friction factor is not affected by the frequency of rotation.

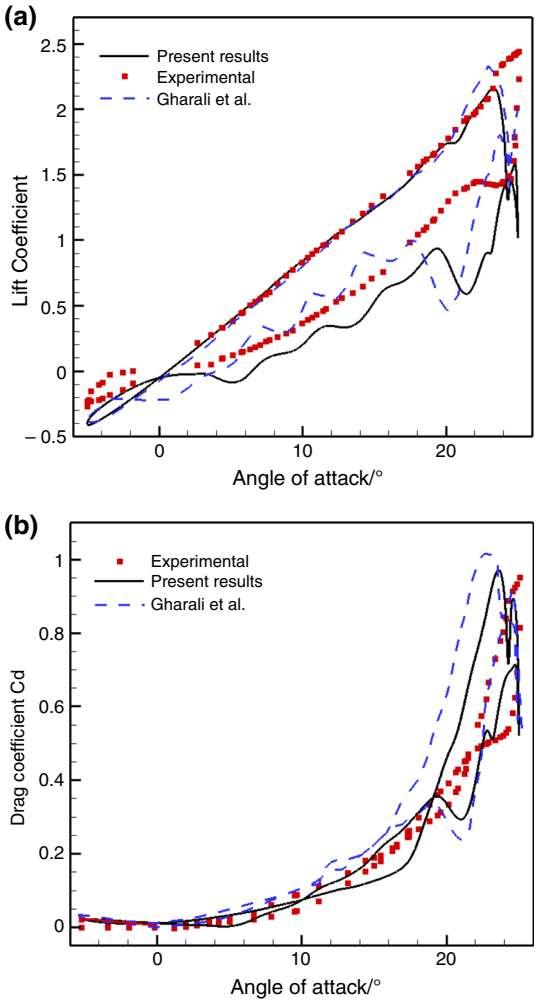

Fig. 4 Comparison of the present lift and drag coefficients with previous experiments and numerical results

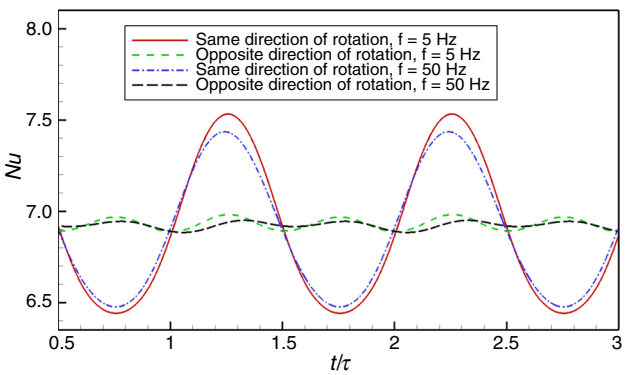

Fig. 5 Nusselt number (*Nu*) for different rotation frequencies and rotation modes (*Re* = 200)

Therefore, its variation is independent of the rotation frequency and only depends on the rotation mode.

Figures 7 and 8 represent the Nusselt number and friction factor for the same direction of rotation with the

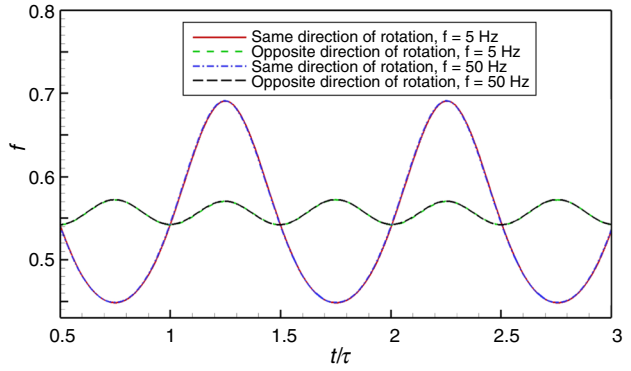

Fig. 6 Friction factor (f) for different rotation frequencies and rotation modes (Re = 200)

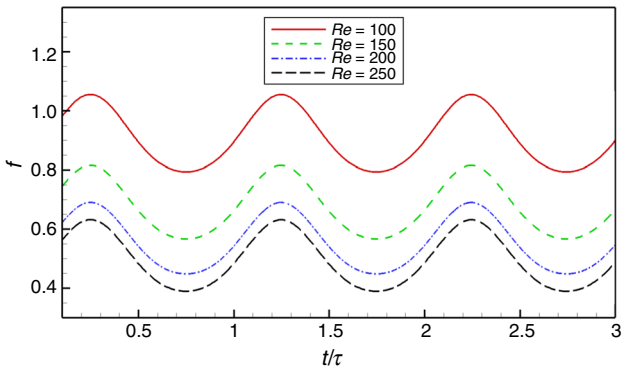

Fig. 8 Friction factor variation with different Re numbers

Table 4 Quantitative data presented in Figs. 5 and 6

Same direction				Opposite direction			
f = 5 Hz		f = 50 Hz		f = 5 Hz		f = 50 Hz	
Nu	f	Nu	f	Nu	f	Nu	f
6.986 ± 0.546	0.569 ± 0.121	6.943 ± 0.424	0.569 ± 0.121	6.954 ± 0.013	0.556 ± 0.014	6.924 ± 0.025	0.556 ± 0.014

frequency of 5 Hz in different Reynolds numbers ranging from 100 to 250. As depicted in Fig. 7 by increasing the Reynolds number, both the average and the amplitude of Nusselt number increase. According to this figure, at low Reynolds numbers (lower than 100), variations of Nusselt number are insignificant. One can conclude that using rotating vortex generators can be recommended in high Reynolds numbers to achieve higher heat transfer rates. Furthermore, it is worthy to note that the local maximum values of Nusselt number and friction factor are coincident with maximum angular position (i.e., 40°).

As can be observed from Fig. 8 by increasing the Reynolds numbers the average value of friction factor increases, but its amplitude remains constant. In other words, by increasing the Reynolds number, the time history curve of friction factor is shifted upward.

Figure 9 represents overall performance (η) of using rotating VGs and nanofluid in the microchannels versus time. Reported results by Ebrahimi et al. [24] are plotted for comparison. As can be seen from this figure, overall performance in Reynolds number of 100, 150, and 200 meets one peak. Moreover, for Re = 250 the overall performance meets two peaks. According to this figure, the overall performance at Reynolds number of 100 is lower than results reported in the literature [24]. However, for higher Reynolds numbers (150, 200 and 250) it can be seen that using rotating vortex generators has enhanced the overall performance.

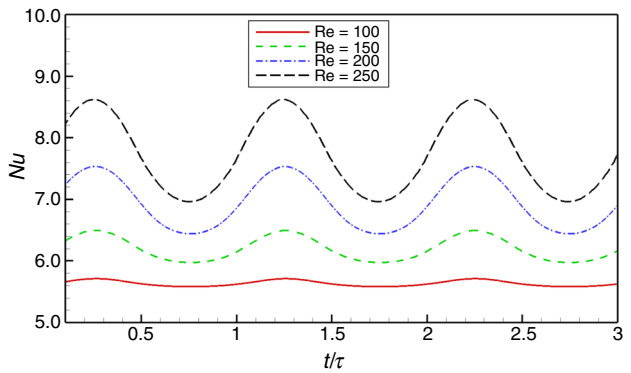

Fig. 7 Nu variation with different Re numbers

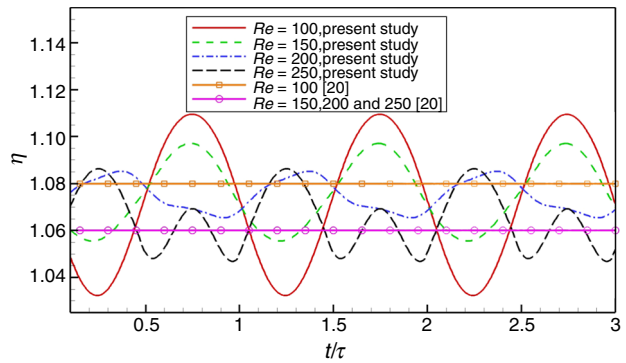

Fig. 9 Overall performance of using rotating VGs in different Reynolds numbers

In Fig. 10, the deformations of the grid during the rotation of VGs are shown. The dimensionless time between two consecutive photos are $\frac{t}{\tau} = 0.15$. As can be seen, during these rotations the grid deforms in a good manner and its quality remains in an acceptable range.

Figure 11a–h depicts the temperature contour during one period of rotation when VGs are rotating in the same direction with 5 Hz of frequency. In this figure, 4th and 5th VGs are displayed for Reynolds of 150. The dimensionless time between two consecutive images is 0.15. This figure shows that the use of rotating VGs has caused much heat propagation in the domain (smoother temperature gradients) leading to higher Nusselt numbers. As can be seen from this figure, when VGs are rotating clockwise (angular position increases), the fluid flowing over the VG accelerates and separates from the surface of VG. As a result, a strong wake region is produced behind the VG. In this region due to strong vortexes, fluid circulates and its temperature increases due to heat conduction from the wall. When the angular position is smaller, the effects of the wake region decrease and fluid temperature behind the VG decrease consequently. Figure 11i illustrates temperature distribution in the same section of microchannel when no VGs are used. As can be seen from this figure, when VGs are used, the temperature distribution is uniform in the middle plane.

Figure 12 represents temperature field in cross sections located immediately after VGs during one period of VGs

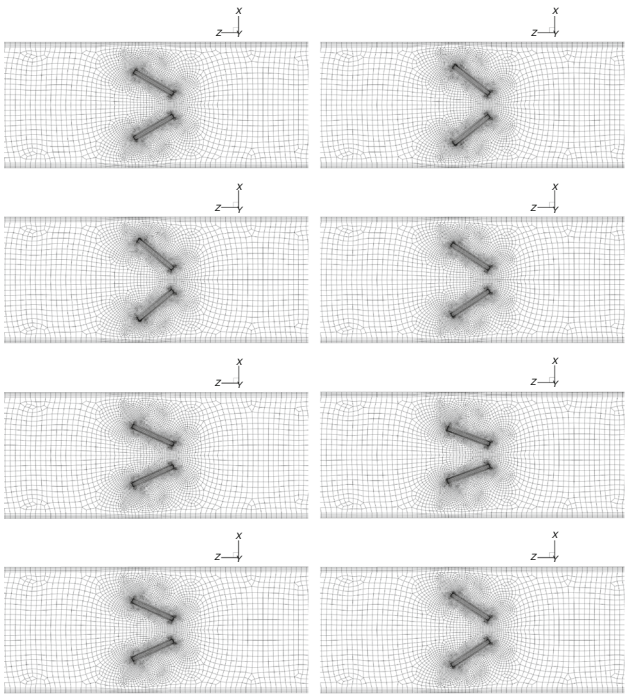

Fig. 10 Deformation of the grid during one period of VGs rotation (dimensionless time between two consecutive images is 0.15)

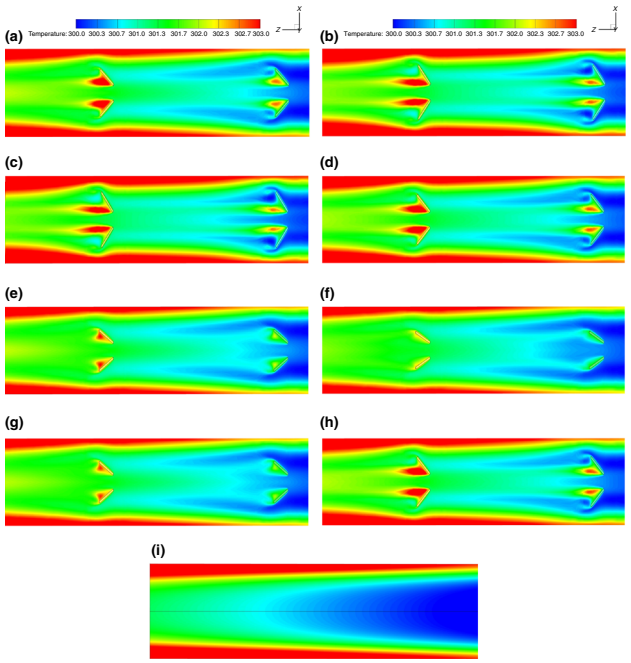

Fig. 11 Temperature contour in the middle plane during one period of VGs rotation (Reynolds number of 150 dimensionless time between two consecutive images is 0.15)

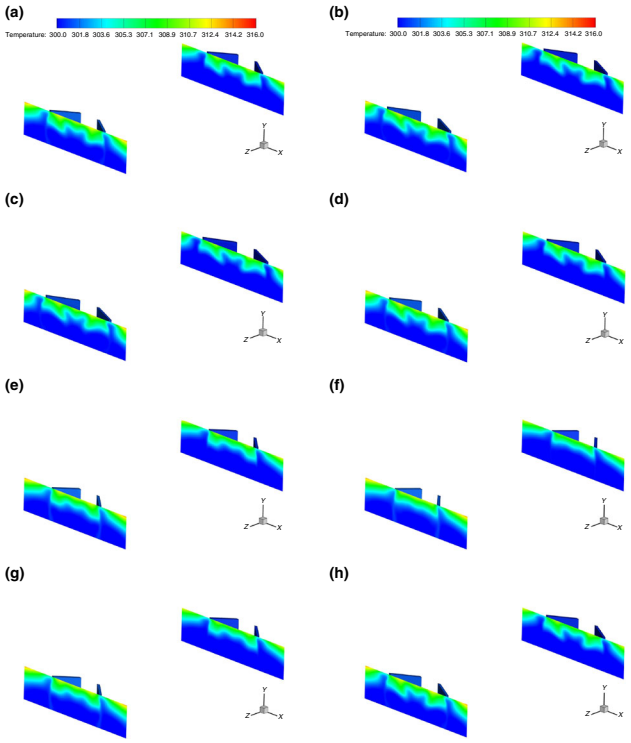

Fig. 12 Temperature contour in cross sections just after VGs during one period of VGs rotation (Reynolds number of 150 dimensionless time between two consecutive images is 0.15)

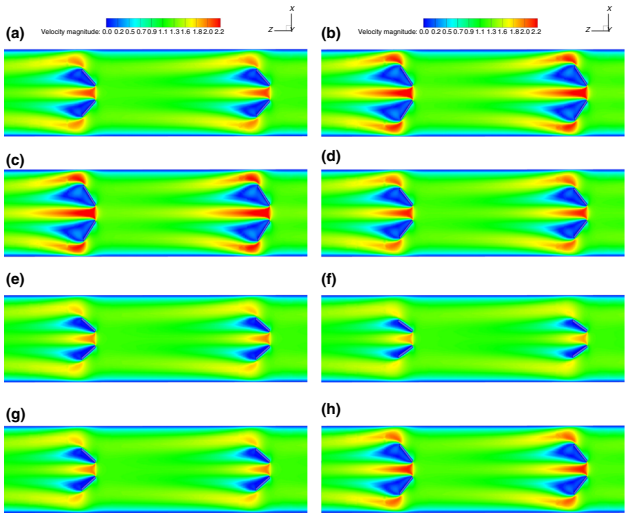

Fig. 13 Temperature contour in the middle plane during one period of VGs rotation (Reynolds number of 150 and dimensionless time between two consecutive images is 0.15)

rotation when VGs are rotating in the same direction with 5 Hz of frequency for Re = 150. According to this figure, VGs rotation increases the area of the high-temperature zone and leads to higher Nusselt number.

Figure 13 shows the velocity contour during one period of VGs rotation when VGs are rotating in the same direction with 5 Hz of frequency. In this figure, 4th and 5th LVGs are displayed for Reynolds number of 150. The dimensionless time between two consecutive images is 0.15. This figure shows that use of rotating VGs changes the maximum velocity near to the wall and between two adjacent VGs. Moreover, the rotation of the VGs has great influence on the vortices behind them. By increasing the angle of VGs with respect to the horizontal line, the vortices size became large and vice versa.

Conclusions

In this study, numerical simulation of three-dimensional flow and conjugated heat transfer in a microchannel involving rotating VGs are presented. Al_2O_3–water as nanofluid with 0.5% volume fraction is used. Different VG's rotation frequencies and Reynolds numbers alongside different rotation modes are considered, and their effects on microchannel thermal and flow performance are studied. The main conclusions are as follows:

- In the same Reynolds number, when VGs are rotating in the same direction, the amplitudes of Nusselt number variations are more significant and more sensitive in comparison with when every other VGs are rotating in the opposite direction. By increasing the rotation frequency, the amplitudes of the Nusselt number decrease. The friction factor is independent of rotation frequency, but it depends on the rotation mode of VGs.
- When VGs are rotating in the same direction, the Nusselt number and friction factor meet one peak in a period. However, when every other VGs are rotating in opposite directions, their variations meet two peaks in a period.
- The frequency of variations of Nusselt number and friction factor are the same as the rotation frequency of VGs in both rotation modes.
- In the case of same rotation direction, by increasing Reynolds number, the amplitude of variation of Nusselt number becomes more substantial. However, the amplitude of variation of friction factor remains constant and is not sensitive to Reynolds number.
- Using rotating vortex generators can increase heat transfer and overall performance of microchannel at high Reynolds numbers.

References

1. Tuckerman DB, Pease RFW. High-performance heat sinking for VLSI. IEEE Electron Device Lett. 1981;2:126–9.
2. Xu B, Ooti K, Wong N, Choi W. Experimental investigation of flow friction for liquid flow in microchannels. Int Commun Heat Mass Transf. 2000;27:1165–76.
3. Toh K, Chen X, Chai J. Numerical computation of fluid flow and heat transfer in microchannels. Int J Heat Mass Transf. 2002;45:5133–41.
4. Wu H, Cheng P. An experimental study of convective heat transfer in silicon microchannels with different surface conditions. Int J Heat Mass Transf. 2003;46:2547–56.
5. Moradikazerouni A, Afrand M, Alsarraf J, Mahian O, Wongwises S, Tran M-D. Comparison of the effect of five different entrance channel shapes of a micro-channel heat sink in forced convection with application to cooling a supercomputer circuit board. Appl Therm Eng. 2019;150:1078–89.
6. Li Z, Tao W-Q, He Y-L. A numerical study of laminar convective heat transfer in microchannel with non-circular cross-section. Int J Therm Sci. 2006;45:1140–8.
7. Dehghan M, Daneshipour M, Valipour MS, Rafee R, Saedodin S. Enhancing heat transfer in microchannel heat sinks using converging flow passages. Energy Convers Manag. 2015;92:244–50.
8. Xia G, Jiang J, Wang J, Zhai Y, Ma D. Effects of different geometric structures on fluid flow and heat transfer performance in microchannel heat sinks. Int J Heat Mass Transf. 2015;80:439–47.
9. Li Y, Xia G, Ma D, Jia Y, Wang J. Characteristics of laminar flow and heat transfer in microchannel heat sink with triangular cavities and rectangular ribs. Int J Heat Mass Transf. 2016;98:17–28.
10. Khoshvaght-Aliabadi M, Baneshi Z, Khaligh S. Analysis on performance of nanofluid-cooled vortex-generator channels with variable longitudinal spacing among delta-winglets. Appl Therm Eng. 2017;122:1–10.

11. Al-Asadi MT, Alkasmoul F, Wilson M. Heat transfer enhancement in a micro-channel cooling system using cylindrical vortex generators. Int Commun Heat Mass Transf. 2016;74:40–7.
12. Ghani IA, Kamaruzaman N, Sidik NAC. Heat transfer augmentation in a microchannel heat sink with sinusoidal cavities and rectangular ribs. Int J Heat Mass Transf. 2017;108:1969–81.
13. Datta A, Sanyal D, Das AK. Numerical investigation of heat transfer in microchannel using inclined longitudinal vortex generator. Appl Therm Eng. 2016;108:1008–19.
14. Ebrahimi A, Roohi E, Kheradmand S. Numerical study of liquid flow and heat transfer in rectangular microchannel with longitudinal vortex generators. Appl Therm Eng. 2015;78:576–83.
15. Mahian O, Kolsi L, Amani M, Estellé P, Ahmadi G, Kleinstreuer C, Marshall JS, Siavashi M, Taylor RA, Niazmand H. Recent advances in modeling and simulation of nanofluid flows-part I: fundamental and theory. Phys Rep. 2018;790:1–48.
16. Subramani J, Nagarajan P, Mahian O, Sathyamurthy R. Efficiency and heat transfer improvements in a parabolic trough solar collector using TiO2 nanofluids under turbulent flow regime. Renew Energy. 2018;119:19–31.
17. Sardarabadi H, Heris SZ, Ahmadpour A, Passandideh-Fard M. Experimental investigation of a novel type of two-phase closed thermosyphon filled with functionalized carbon nanotubes/water nanofluids for electronic cooling application. Energy Convers Manag. 2019;188:321–32.
18. Chamkha AJ, Molana M, Rahnama A, Ghadami F. On the nanofluids applications in microchannels: a comprehensive review. Powder Technol. 2018;332:287–322.
19. Kumar N, Singh P, Redhewal AK, Bhandari P. A review on nanofluids applications for heat transfer in micro-channels. Procedia Eng. 2015;127:1197–202.
20. Wang Z, Wu Z, Han F, Wadsö L, Sundén B. Experimental comparative evaluation of a graphene nanofluid coolant in miniature plate heat exchanger. Int J Therm Sci. 2018;130:148–56.
21. Khoshvaght-Aliabadi M, Deldar S, Hassani S. Effects of pin-fins geometry and nanofluid on the performance of a pin-fin miniature heat sink (PFMHS). Int J Mech Sci. 2018;148:442–58.
22. Mahian O, Kolsi L, Amani M, Estellé P, Ahmadi G, Kleinstreuer C, Marshall JS, Taylor RA, Abu-Nada E, Rashidi S. Recent advances in modeling and simulation of nanofluid flows-part II: applications. Phys Rep. 2018;791:1–59.
23. Ambreen T, Kim M-H. Effects of variable particle sizes on hydrothermal characteristics of nanofluids in a microchannel. Int J Heat Mass Transf. 2018;120:490–8.
24. Ebrahimi A, Rikhtegar F, Sabaghan A, Roohi E. Heat transfer and entropy generation in a microchannel with longitudinal vortex generators using nanofluids. Energy. 2016;101:190–201.
25. Sabaghan A, Edalatpour M, Moghadam MC, Roohi E, Niazmand H. Nanofluid flow and heat transfer in a microchannel with longitudinal vortex generators: two-phase numerical simulation. Appl Therm Eng. 2016;100:179–89.
26. Nitiapiruk P, Mahian O, Dalkilic AS, Wongwises S. Performance characteristics of a microchannel heat sink using TiO_2/water nanofluid and different thermophysical models. Int Commun Heat Mass Transf. 2013;47:98–104.
27. Tafarroj MM, Mahian O, Kasaeian A, Sakamatapan K, Dalkilic AS, Wongwises S. Artificial neural network modeling of nanofluid flow in a microchannel heat sink using experimental data. Int Commun Heat Mass Transf. 2017;86:25–31.
28. Bhattacharya P, Samanta A, Chakraborty S. Numerical study of conjugate heat transfer in rectangular microchannel heat sink with Al_2O_3/H_2O nanofluid. Heat Mass Transf. 2009;45:1323–33.
29. Ho C-J, Wei L, Li Z. An experimental investigation of forced convective cooling performance of a microchannel heat sink with Al_2O_3/water nanofluid. Appl Therm Eng. 2010;30:96–103.
30. White FM. Fluid mechanics. 5th ed. Boston: McGraw-Hill Book Company; 2003.
31. Lee P-S, Garimella SV. Thermally developing flow and heat transfer in rectangular microchannels of different aspect ratios. Int J Heat Mass Transf. 2006;49:3060–7.
32. Bergman TL, Incropera FP, DeWitt DP, Lavine AS. Fundamentals of heat and mass transfer. Hoboken: Wiley; 2011.
33. Glassbrenner C, Slack GA. Thermal conductivity of silicon and germanium from 3 K to the melting point. Phys Rev. 1964;134:A1058.
34. Yue Y, Mohammadian SK, Zhang Y. Analysis of performances of a manifold microchannel heat sink with nanofluids. Int J Therm Sci. 2015;89:305–13.
35. Pak BC, Cho YI. Hydrodynamic and heat transfer study of dispersed fluids with submicron metallic oxide particles. Exp Heat Transf Int J. 1998;11:151–70.
36. Koo J, Kleinstreuer C. A new thermal conductivity model for nanofluids. J Nanopart Res. 2004;6:577–88.
37. Hamilton R, Crosser O. Thermal conductivity of heterogeneous two-component systems. Ind Eng Chem Fundam. 1962;1:187–91.
38. Li J. Computational analysis of nanofluid flow in microchannels with applications to micro-heat sinks and bio-MEMS. Ph.D. Thesis, NC State University, Raleigh, NC, the United States (2008).
39. Kalteh M, Abbassi A, Saffar-Avval M, Frijns A, Darhuber A, Harting J. Experimental and numerical investigation of nanofluid forced convection inside a wide microchannel heat sink. Appl Therm Eng. 2012;36:260–8.
40. Li P, Zhang D, Xie Y. Heat transfer and flow analysis of Al 2 O 3–water nanofluids in microchannel with dimple and protrusion. Int J Heat Mass Transf. 2014;73:456–67.
41. Zhai Y, Xia G, Liu X, Li Y. Heat transfer in the microchannels with fan-shaped reentrant cavities and different ribs based on field synergy principle and entropy generation analysis. Int J Heat Mass Transf. 2014;68:224–33.
42. Lee T, Gerontakos P. Investigation of flow over an oscillating airfoil. J Fluid Mech. 2004;512:313–41.
43. Gharali K, Johnson DA. Dynamic stall simulation of a pitching airfoil under unsteady freestream velocity. J Fluids Struct. 2013;42:228–44.